ELSEVIER

Contents lists available at ScienceDirect

Earth and Planetary Science Letters

journal homepage: www.elsevier.com/locate/epsl



Deep root activity overprints weathering of petrogenic organic carbon in shale



Alison K. Tune ^a, Jennifer L. Druhan ^{b,c}, Corey R. Lawrence ^d, Daniella M. Rempe ^{a,*}

- ^a Jackson School of Geosciences, Univ. of Texas at Austin, 78712, USA
- ^b Department of Geology, Univ. of Illinois at Urbana-Champaign, 61801, USA
- ^c Institut de Physique du Globe de Paris, Sorbonne Paris Cité, Université Paris Diderot, CNRS, Paris, 75238, France
- d U.S. Geological Survey, Denver, 80225, USA

ARTICLE INFO

Article history:
Received 9 September 2022
Received in revised form 6 January 2023
Accepted 6 February 2023
Available online 3 March 2023
Editor: A. Jacobson

Dataset link: http:// www.hydroshare.org/resource/ 82a50af377e14df0bdb994a982b24634

Dataset link: https://doi.org/10.5281/zenodo.7619193

Keywords: radiocarbon petrogenic organic carbon weathering rates

ABSTRACT

The oxidation of organic carbon in sedimentary bedrock (petrogenic OC, OCpetro) is increasingly recognized as a potential source of CO2 to the atmosphere. Recent studies provide evidence for the mobilization and oxidation of OCpetro in sedimentary bedrock during rock weathering. However, the mechanisms and rates remain uncertain, particularly where overlying soils and vegetation drive contemporaneous oxidation of recently fixed organic carbon. Here, we quantify OC_{netro} weathering across a 16 m shale depth profile in a steep, rapidly eroding forested hillslope in the Northern California Coast Ranges. We report solid and gas phase radiocarbon and stable isotope analyses of samples extracted from specialized in-situ samplers, and a supporting laboratory incubation experiment of the shale regolith. OC_{netro} is removed from the weathered bedrock at a rate of approximately 0.12 gC/m³yr, which is orders of magnitude lower than the rate of OCpetro oxidation we achieved in the laboratory with crushed samples (557.1 gC/m³/yr). This disparity occurs despite high $O_{2(g)}$ content across the depth profile, indicating that physical accessibility of OCpetro can regulate oxidative weathering. There is no direct radiocarbon evidence of OC_{petro} oxidation in $CO_{2(g)}$ across the upper 13 m of the weathering profile during both wet and dry seasons. Instead, vadose zone $CO_{2(g)}$ production at the site is dominated by respiration of recently fixed carbon associated with deep rooting. OCpetro is clearly mobilized across the vadose zone during weathering in this rapidly eroding, oxygen-rich, biologically dynamic hillslope, but at rates far below what can be measured given the contribution of root-derived $CO_{2(g)}$.

© 2023 Elsevier B.V. All rights reserved.

1. Introduction

Earth's climate is sensitive to carbon fluxes associated with bedrock weathering over geologic timescales (Hilton and West, 2020). Organic carbon within sedimentary rocks, here termed petrogenic organic carbon (OC_{petro}), serves as a source of CO_2 to the atmosphere when oxidized (e.g. Keller and Bacon, 1998; Petsch et al., 2000; Bouchez et al., 2010; Soulet et al., 2018; Hemingway et al., 2018; Horan et al., 2019; Hilton and West, 2020; Soulet et al., 2021). However, the controls on OC_{petro} oxidation rates and their sensitivity to climatic and tectonic perturbation are poorly constrained due to uncertainty regarding the mechanisms of OC_{petro} weathering, i.e. the overall mobilization and loss of OC_{petro} from rock.

It has been proposed that OCpetro oxidation rates are generally rapid where erosion rates are high (Hemingway et al., 2018; Hilton et al., 2021) but direct testing of these inferences is impeded by the presence of photosynthetically derived, recently fixed carbon associated with rhizosphere processes, which complicate interpretation of radiocarbon signatures. Feedbacks between pathways of modern and OCpetro oxidation are presently poorly constrained (Petsch et al., 2001; Hemingway et al., 2018). Where cycling of modern carbon is driven by roots and rhizosphere processes, OC_{petro} mobilization and susceptibility to oxidation may become enhanced due to accelerated mineral dissolution rates (Wen et al., 2021) and/or nutrient acquisition by roots (Murphy et al., 2015). Alternatively, OCpetro oxidation could be modulated by an active rhizosphere rich in labile low molecular weight organics, consumption of $O_{2(g)}$ in surface soils, preservation of anaerobic conditions in microporous shales (LaRowe and Van Cappellen, 2011), protection through clay sorption and other soil physiochemical characteristics (Rasmussen et al., 2018), or occlusion in small

^{*} Corresponding author.

E-mail address: rempe@jsg.utexas.edu (D.M. Rempe).

pore spaces that restrict microorganism or oxygen access (Tecon and Or, 2017).

Constraining the relationship between OC_{petro} weathering and rhizosphere activity is necessary in uplifting and eroding land-scapes where substantial biomass exists and is projected to increase as treelines move higher in elevation and latitude (Hansson et al., 2021; Sharma et al., 2022). Warming alone may also accelerate OC_{petro} weathering because oxidation rates measured in exposed sedimentary rocks scale with temperature (Soulet et al., 2021). These observations raise questions as to the potential acceleration of OC_{petro} oxidation associated with climate change, raising uncertainty around what is already a poorly constrained flux of atmospheric CO_2 .

To date, OCpetro oxidation has been documented using radiocarbon measurements in soils (Hemingway et al., 2018) and exposed OC-bearing rock outcrops (Soulet et al., 2018, 2021; Roylands et al., 2022). At the watershed scale, indirect evidence of oxidation comes from dissolved rhenium in streamflow (e.g. Horan et al. (2017, 2019); West et al. (2019); Hilton et al. (2021)). Comparatively little is known about the processes operating in active weathering profiles. Here, we leverage unique in-situ observations to investigate controls on OCpetro weathering and oxidation within a rapidly uplifting (0.2 mm/yr, Fuller et al. (2009)) OC-rich (0.6 wt%, Gu et al. (2020)) argillite weathering profile in a forested hillslope in Northern California. Previous studies report deep rooting within the weathering profile (Rempe and Dietrich, 2018), evidence of substantial oxidation of OC within the weathered bedrock (Tune et al., 2020), and depletion of OCpetro across vertical cores (Gu et al., 2020). Therefore, this is a system that appears likely to support substantial rates of OC_{netro} weathering. In this context, we address the following questions:

- What fraction of CO_{2(g)} generated within the hillslope interior is sourced from OC_{petro}?
- 2. What is the maximum rate at which OC_{petro} can be oxidized from this bedrock?
- 3. How does the in situ rate of OC_{petro} removal compare to the maximum possible rate and what limits loss within the hillslope?

Through a combination of laboratory incubations, solid and gaseous phase radiocarbon analyses, aqueous phase carbon isotope analyses, and solid phase elemental chemical analysis, we seek to quantify the controls on OC_{petro} mobilization and oxidation during active weathering.

2. Methods

2.1. Study area

The study site is an intensively instrumented, steep (approximately 32°) 4000 m² hillslope, which we refer to as "Rivendell", in the Eel River Critical Zone Observatory (ERCZO) (Fig. 1). Rivendell drains to the 16.8 km² Elder Creek watershed, which is a tributary to the South Fork of the Eel River in north-central California. The bedrock at the site is mapped as the Eocene Yager terrane of the Coastal Belt of the Franciscan Complex (Ernst and McLaughlin, 2012) which contains turbidite sequences of shales, sandstones, and conglomerates that were buried to depths of less than 5–8 km in the subduction zone and experienced only low-grade metamorphism (Ernst and McLaughlin, 2012).

The Rivendell hillslope is underlain primarily by argillaceous shale with some minor arkosic graywacke and conglomerate interbeds. Modern erosion rates in the South Fork of the Eel River watershed are approximately 0.1-0.3 mm/yr and during the Pleistocene, erosion rates may have been as high as 0.3-0.4 mm/yr

(Fuller et al., 2009). In the Elder Creek catchment, modern erosion rates are slightly higher at 0.28 mm/yr, possibly due to deep-seated landslides (Fuller et al., 2009). The argillite parent bedrock at Rivendell contains quartz (24.8 wt%), albite (21.9 wt%), chlorite (18.3 wt%), smectite (12.6 wt%), illite (7.4 wt%), kaolinite (3.5 wt%), and carbonate (2.2 wt%) minerals, as well as organic carbon (0.6 wt%) (Gu et al., 2020). Soils across the hillslope are thin (0.5-0.75 m). The underlying bedrock is deeply weathered at the hillslope divide (25 m) and the thickness of weathering decreases downslope to approximately 4 m near the channel (Rempe and Dietrich, 2014). Carbonate dissolution and pyrite oxidation fronts approximately coincide with the base of the weathering profile and are associated with a sharp change in porosity (Gu et al., 2020). Inorganic carbon contributions from carbonate solubilization and sulfide oxidation are considered further below.

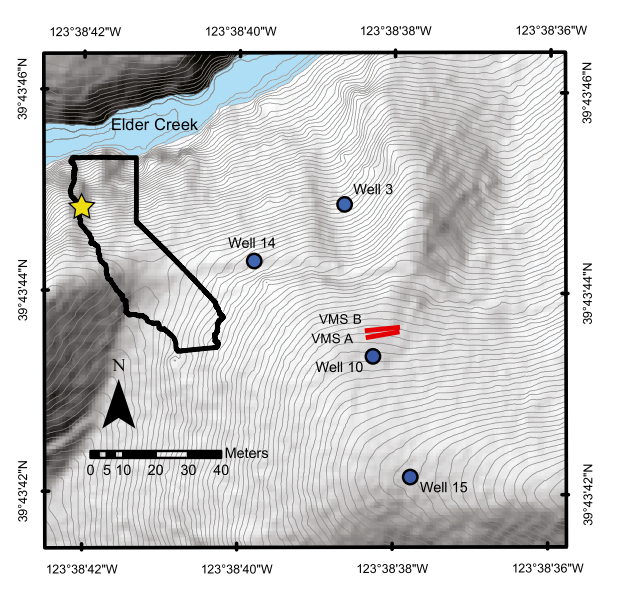
The Mediterranean climate of the site is characterized by cool, wet winters and warm, dry summers. Nearly all precipitation occurs as rain within a 5-6 month window (December to May). The mean annual precipitation is 1,800 mm/yr, mean annual temperature is 13 °C and daily average temperatures range from 0 (December) to about 20 °C (August) (Salve et al., 2012; Hahm et al., 2019). The old-growth forest canopy is composed of a mix of Douglas-fir (Pseudotsuga menziesii), Pacific madrone (Arbutus menziesii), tan oak (Notholithocarpus densiflorus), and live oaks (Quercus wislizeni and Q. chrysolepis) with very little understory.

2.2. Gas sampling and analysis

Gas samples are collected from a unique Vadose Zone Monitoring System (VMS), which is comprised of sensors and samplers installed within two inclined boreholes that traverse the length of the weathering profile (Fig. 1). Discrete water and gas samplers are distributed throughout the unsaturated, fractured bedrock. At Rivendell, the VMS is comprised of two parallel units with one containing perforated gas sample tubing embedded within 10 passive suction lysimeters that are each 1.25 m long. The other VMS sleeve houses flexible time-domain-transmission (TDT) sensors which measure temperature and water content. Most VMS ports are within the unsaturated zone, but some are located below the water table and therefore sample groundwater (see Table S1 in Tune et al., 2020). The Rivendell VMS is described in Tune et al. (2020) and the functioning of the VMS samplers are described in Turkeltaub et al. (2015) and Dahan et al. (2009).

Sample collection for CO_2 , O_2 , and CO_2 carbon isotopes occurred during September 2018 and March 2019 to encapsulate seasonal variations in subsurface water content. In September, water contents throughout the bedrock vadose zone are at a minimum after months of little to no precipitation. In March, water contents are near a maximum. $CO_{2,(g)}$ and $O_{2,(g)}$ were measured in the field using a Quantek Instruments Oxygen and Carbon Dioxide Analyzer (Model 902P) by pumping gas at approximately 300 cc/s through the gas sampling tubing in the VMS. The O_2 sensor was calibrated before and during each sampling campaign. The CO_2 sensor was calibrated by Quantek Instruments. Measurement errors are $\pm 0.2\%$.

Samples for radiocarbon analysis were collected in evacuated, 400 ml canisters by pumping air from the VMS using the Quantek until CO₂ concentrations stabilized, turning off the pump and closing off the tubing to the pump, and then opening the sampling container to collect the pore space gas from the sampling line. Duplicate samples were collected at two depths during each of the sampling campaigns. After equilibrating, the sample container was closed, stored for transport, and analyzed at the University of California, Irvine at the Keck Carbon Cycle AMS facility. Carbon yields ranged from 1.1 to 5.8 mg-C. Fraction modern carbon, F_m, values in Table 5 were corrected for ¹³C as reported by the UC Irvine AMS facility.



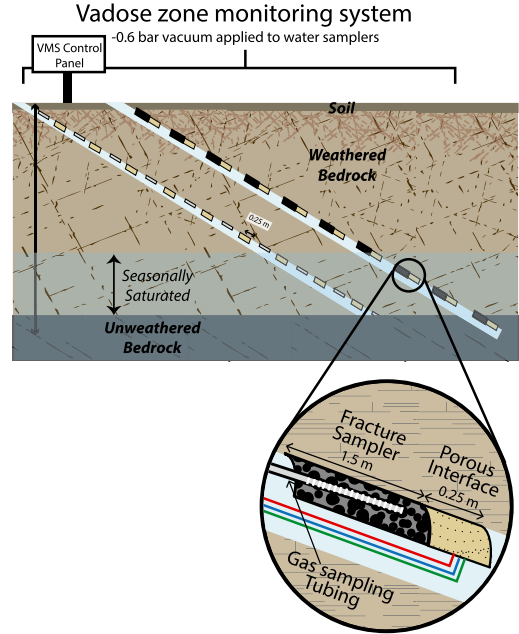


Fig. 1. Location of the vadose zone monitoring system (VMS) and wells in the Rivendell hillslope. Well 15 is located at the ridge of the hillslope, well 10 is near the VMS, and wells 14 and 3 are located mid-slope. A schematic of the VMS is shown to the right, with the sampling port construction illustrated as an inset. The figure is adapted from (Tune et al., 2020).

2.3. Solid phase geochemical analysis

Solid samples were obtained from the material recovered during drilling and installation of the VMS in October 2015. Subsamples were analyzed for carbon isotopes at the University of California, Irvine at the Keck Carbon Cycle AMS facility. Separate (\sim 50 grams each) subsamples were analyzed for concentrations of major oxides, minor elements, organic and total carbon, and sulfur at Bureau Veritas, Inc (Canada). Samples were first dried and sieved to an 80-mesh for disaggregated samples and a 200-mesh for pulverized rock samples. Volatile content such as organic matter was determined by loss on ignition (LOI). Elemental composition was characterized using inductively coupled plasma emission spectroscopy (Spectro Ciros/Arcos) after lithium-borate fusion and dissolution in nitric acid. Total C and S were determined using an elemental analyzer (LECO CS230). Organic carbon was reported as the total carbon less graphite carbon and CO₂.

Samples of solids from wells 3, 10, 14, and 15 were also analyzed for major oxides, minor elements, organic and total C and S and the results are published in Gu et al. (2020).

2.4. Determining OC_{petro} content in the solid phase

A binary source model (Hemingway et al., 2018) was used to constrain the maximum amount of OC_{petro} (X_{petro}) that could contribute to the observed ¹⁴C concentrations in the solid phase ($^{14}C_{solid}$):

$$X_{petro} = 1 - \frac{F_m}{F_{bio}} \tag{1}$$

Here F_m is the fraction modern carbon in a sample at a depth of interest, and F_{bio} is the fraction modern of recently biologically produced OC. We did not directly measure F_{bio} and assume F_{bio} = 1.03314, the highest $^{14}\text{CO}_{2,resp}$ constrained by our diffusion model (see Section 2.7 and Fig. 3). F_m is converted to $\Delta^{14}C$ using Equation (2), which is derived from Stuiver and Polach (1977)

$$\Delta^{14}C = (F_m e^{(1950 - y)/8267} - 1) * 1000$$
 (2)

where y is the year the samples were measured (2018 or 2019).

2.5. Solid phase porosity and bulk density

Samples recovered via drilling were a mixture of chips of rock and fine grained material. Analysis of bulk density and matrix porosity was limited to competent chips of rock. Thus, these measurements exclude the porosity associated with the fractures or any fine grained weathering products that occupy fractures. We used a helium pycnometer (Micromeritics AccuPyc II 340) and an envelope density analyzer (Micromeritics GeoPyc 1360) to measure effective porosity, grain density, and bulk density. Duplicate measurements of the same sample showed a standard deviation of 1.1% while repeat measurements of different samples from the same depth showed a standard deviation of 1.5% (Pedrazas et al., 2021). We estimate the porosity due to fractures beneath 8 m to be 5% (Gu et al., 2020) and calculate the total bulk density (ρ_T) as:

$$\rho_T = 0.95 \left(\frac{\rho_A + \rho_G}{2} \right) + 0.05 \tag{3}$$

where ρ_T is the total bulk density including the assumed fracture porosity, ρ_A is the bulk density from the AccuPyc method, and ρ_G is the bulk density from the GeoPyc method.

2.6. Rates of OC_{petro} weathering

From this point forward, we use the term " OC_{petro} weathering" to encapsulate all pathways by which OC_{petro} is removed from the solid phase across the in-situ weathering profile, i.e. before weathered bedrock is incorporated into shallow soils. This includes both oxidation (conversion to CO_2) and solubilization mechanisms, and is consistent with the sustained release of organic matter from sedimentary rocks documented in prior flow-through column experiments (Schillawski and Petsch, 2008). We use the solid phase OC concentrations from two deep VMS samples (12.9 and 16.1 m) to calculate the rate at which OC_{petro} is weathered from bedrock. The radiocarbon content of both samples is extremely low ($\Delta^{14}C$ <

-900‰), indicating that modern surface inputs are negligible. The weathering rate (R_{loss}) in $gC/m^3/yr$ is then the product of the rock uplift rate (ϵ , m/yr) and the difference in OC concentration (weight fraction multiplied by bulk density, ρ_b gC/m^3) divided by the distance between the two samples (ΔZ , m). This is equivalent to normalizing the difference in OC concentration between two depths to the time the rock spent transiting that distance, assuming a steady state uplift rate. The same calculation is applied to deep samples from several of our wells (Fig. S1), however, radiocarbon content is not available to confirm negligible input from surface derived OC in these samples.

In addition to R_{loss} , we report the mass depletion of OC (τ_{OC}) throughout the weathering profile (Eq. (4)). To calculate τ_{OC} , we reference changes in concentration of the mobile element (OC) to an assumed immobile element (Ti), while accounting for weathering derived changes in element concentrations.

$$\tau_{OC} = \frac{C_{OC,w}C_{Ti,p}}{C_{OC,p}C_{Ti,w}} - 1 \tag{4}$$

where C is the concentration (weight percent) in the parent (p) or weathered (w) rock. We use the analysis of blanks to propagate error through Equation (4). Loss of OC is signified by negative values of τ_{OC} and enrichment is signified by positive values of τ_{OC} . The deepest VMS sample (16.1 m) is used to represent the parent rock for our τ_{OC} calculation, because it is located below the carbonate weathering front, contains pyrite, and shows negligible radiocarbon. We also report the parent rock OC concentration averaged across several wells and the stream bed by Gu et al. (2020), but we elect to use our deep VMS sample in Eq. (4) because we can directly confirm negligible surface derived OC via radiocarbon analysis.

2.7. Shale incubation experiments

Incubation experiments were conducted on weathered bedrock samples. Following the incubation procedure of Liu et al. (2019), gas-tight valves were installed in 473 mL glass jars using polyethylene tubing through bulkhead fittings in the lids. Leakage during and prior to the experiment was tested with CO₂-free air. Visible roots were removed, but beyond this no further interventions were employed to mitigate microbial activity. This is consistent with common practice in soil incubation studies and allows for naturally occurring biomass to contribute to the oxidation of labile OC. Mixed size samples were crushed in order to increase surface area and promote oxidation. Samples that contained only rock chips were blown clean with compressed air to remove fine particles on the surface and then crushed. Sufficient water was added to achieve 60% (w/w) saturation. On average, incubation vessels contained 442 mL of headspace and 8 mL of water, i.e. a large air:water ratio.

Headspace CO_2 was analyzed using a gas analyzer (EGM-5 CO_2 Gas Analyzer, PP Systems, Amesbury, MA, USA) at a higher frequency early in the experiment when CO_2 accumulation was fast and a decreasing frequency later in the experiment when CO_2 accumulation was slower. The entire incubation lasted over a period of two weeks. After each measurement of the headspace, the incubation chamber was purged with CO_2 -free air before sealing for the next analysis.

2.8. Estimating the maximum contribution of oxidized OC_{petro} to total $CO_{2,(g)}$

 $\mathsf{CO}_{2,(g)}$ concentrations and isotopic compositions collected from the VMS reflect a combination of $\mathsf{CO}_{2,(g)}$ produced at the point of sample collection and that which has diffused from other depths.

Hence, for each depth measured, it is necessary to constrain (1) the amount and isotopic composition of measured $CO_{2,(g)}$ that was produced (i.e., respired) at each depth and (2) the maximum possible fraction of that respired $CO_{2,(g)}$ that is attributable to OC_{petro} sources. A diffusion-reaction model is applied for the first task (Eq. (5)) and a binary source model (Eq. (1)) is used for the second. Inorganic carbon contributions to $CO_{2,(g)}$ via sulfide oxidation and/or carbonate weathering are considered negligible above the weathering fronts of these minerals (section 3.1).

2.8.1. Diffusion model for ¹⁴C of respired CO₂

The diffusion-reaction model (Eq. (5)) we employ to constrain ¹⁴C activity of respired CO₂ produced at a given depth is based on an analytical solution developed by Davidson (1995), which embeds the original formulations by Cerling (1984) and later extended by Egan et al. (2019) for ¹³C and CO₂. The approach was designed for soil (Egan et al., 2019) and relies on a set of assumptions which have been applied extensively in soil profiles (e.g. Breecker et al. 2012). These are as follows: (1) CO₂ production decreases exponentially with depth, (2) there is a lower no-flux boundary condition, and (3) the CO₂ profile is at steady state, leading to an increase in CO₂ concentration with depth (Cerling, 1984). The result is that the model only uses the atmospheric CO2 value and the CO₂ value at the depth of interest (sampled in the field) to calculate the value of respired CO₂ at a given depth, However, it cannot be applied where concentration gradients are complicated by violations of these underlying assumptions. In the VMS, this means that we cannot apply the model across the entire 16 meter weathered bedrock profile. Only the upper 7 m of the unsaturated, weathered bedrock profile show a consistent increase in CO_{2.(g)} concentration with depth (Fig. 2) which adequately resembles concentration profiles in soil, albeit over a larger length scale and in more structured material (weathered rock).

The model can be applied to $CO_{2,(g)}$ concentrations as well as the isotope ratios $\delta^{13}CO_{2,(g)}$ and $\Delta^{14}CO_{2,(g)}$. The latter is possible due to the slow rate of radioisotope decay (half life of 14C 8267 yrs) compared to the rate of gas transport. The approach essentially unmixes atmospheric sources from local production by correcting the bulk measurement for diffusive transport to constrain the respired CO₂ produced at a given depth. The result encapsulates all potential respiration pathways (e.g. root respiration, microbial respiration, OCpetro respiration, and respiration of OC of varying ages). As will be shown below, the isotopic signatures of $CO_{2,(g)}$ do not suggest appreciable inorganic carbon contributions. The assumptions necessary for other widely applied diffusion models (e.g. Davidson and Trumbore (1995)) also incorporate exponential decline in production with depth (Cerling, 1984) and are violated in portions of the profile where CO2, diffusion coefficient (D), and/or ¹⁴C concentrations are very similar between depths. This is the case for the majority of the VMS with respect to D and ¹⁴C (Fig. 2). Therefore, we adhere to the simpler methods outlined by Egan et al. (2019).

The model of ^{14}C transport from Egan et al. (2019) was used to determine the ^{14}C of respired CO₂:

$$\delta_{J}^{14} = \frac{C_{s}(\delta^{14}C_{s} - 8.8) - C_{a}(\delta^{14}C_{a} - 8.8)}{1.0088(C_{s} - C_{a})}$$
 (5)

where δ_J^{14} is the radiocarbon delta value of the respired CO₂ after accounting for diffusion, C_s and C_a are the CO₂ concentrations in the soil gas and atmosphere, respectively, $\delta^{14}C_s$ and $\delta^{14}C_a$ are the radiocarbon delta values of the soil gas and atmosphere, and 1.0088 and 8.8 are constants that account for the differences in mass, and therefore diffusion, of ¹⁴C compared to ¹²C. We apply this model to the concentrations and radiocarbon values of each of the ports (C_s, $\delta^{14}C_s$) for the two gas phase sampling campaigns.

Table 1Parameters used to determine the saturation-dependent diffusion coefficient for modeling.

Well 7 Sample Depth (m)	Equivalent Depth in VMS (m)	Well 7 θ_{May}^{a} (-)	Well 7 $\theta_{Oct.}^{a}$ (-)	$\phi_{epoxy}^{\ \ b}$ (-)	Well 7 min. ϕ_{total} $(\theta_{max} + \phi_{epoxy})$ (-)	$\phi_{air,May}$ estimate (-)	$\phi_{air,0ct.}$ estimate (-)	VMS Temp. Mar. (°C)	VMS Temp. Sept. (°C)	D_{Mar} (m^2/s)	D_{Sept} (m^2/s)
1.6	1.4	0.195	0.138	0.05	0.245	0.05	0.11	8.3	14.26	4.81E-07	1.06E-06
2.7	3.0	0.153	0.098	0.05	0.203	0.05	0.11	11.57	11.6	4.91E-07	1.04E-06
4.1	4.5	0.158	0.094	0.05	0.208	0.05	0.11	10.59	12.64	4.88E-07	1.12E-06
5.4	6.1	0.133	0.147	0.05	0.197	0.06	0.05	11.47	11.73	6.27E-07	4.92E-07

^a Values from Schmidt and Rempe (2020).

Table 2Weathered bedrock chemistry at the VMS.

Depth ^a (m)		Ti (wt%)	Organic Carbon (wt%)	Total Carbon (wt%)	Total Sulfur (wt%)	Tau OC (τ_{OC})
0.5	Above the water table year-round	0.47	0.77	0.83	BDL	0.95 ± 0.06
1.4	Above the water table year-round	0.50	0.35	0.4	BDL	-0.16 ± 0.08
2.2	Above the water table year-round	0.49	0.17	0.22	BDL	-0.58 ± 0.13
2.8	Above the water table year-round	0.49	0.14	0.18	BDL	-0.65 ± 0.15
3.4	Above the water table year-round	0.52	0.21	0.26	BDL	-0.52 ± 0.11
4.1	Above the water table year-round	0.53	0.24	0.28	BDL	-0.45 ± 0.10
4.7	Above the water table year-round	0.51	0.38	0.42	BDL	-0.11 ± 0.08
5.3	Above the water table year-round	0.50	0.32	0.37	BDL	-0.24 ± 0.08
6.1	Above the water table year-round	0.48	0.15	0.18	BDL	-0.63 ± 0.14
6.7	Above the water table year-round	0.45	0.12	0.16	BDL	-0.68 ± 0.18
7.5	Above the water table year-round	0.47	0.18	0.22	BDL	-0.54 ± 0.12
8.1	Within the water table fluctuation zone	0.47	0.18	0.22	BDL	-0.54 ± 0.12
9.1	Within the water table fluctuation zone	0.49	0.28	0.35	BDL	-0.31 ± 0.09
10.3	Within the water table fluctuation zone	0.47	0.37	0.41	BDL	-0.06 ± 0.08
11.5	Within the water table fluctuation zone	0.47	0.29	0.33	BDL	-0.27 ± 0.09
12.9	Within the water table fluctuation zone	0.46	0.28	0.32	BDL	-0.26 ± 0.09
14.0	Within the water table fluctuation zone	0.46	0.32	0.36	BDL	-0.17 ± 0.08
15.1	Within the water table fluctuation zone	0.47	0.37	0.53	0.08	-0.06 ± 0.08
15.6	Below the water table year-round	0.46	0.37	0.5	0.18	-0.04 ± 0.08
16.1	Below the water table year-round	0.47	0.39	0.56	0.10	0 ± 0.07
Stream bed ^b		0.49	$0.59~(\pm~0.15)$	0.71	0.1	0.21

BDL = Below Detection Limit

To approximate the value of $\delta^{14}C_a$ and $\delta^{13}C_a$ in September 2018 ($C_{a,Sept}$) and March 2019 ($C_{a,Mar}$) in Northern California, the observations of Graven et al. (2017) from 2000-2015 in the Northern Hemisphere were linearly extrapolated to 2018.5 and 2019, resulting in $\Delta^{14}C_a$ values of 1.14 and -1.23 and $\delta^{13}C_a$ values of -8.51 and -8.52, respectively. $C_{a,Sept}$ was 408 ppm and $C_{a,Mar}$ was 410 ppm. Conversion between $\Delta^{14}C$ and $\delta^{14}C$ (Eq. (6)) is derived from Eq. 4 in Donahue et al. (1990) and Eqs. in Table 1 of Stuiver and Polach (1977). $\delta^{14}C$ is required for these calculations because $\Delta^{14}C$ is corrected for the $\delta^{13}C$ of the sample, which is also subject to diffusive transport at a different rate due to differences in mass.

$$\delta^{14}C = \left[\left(\frac{\Delta^{14}C}{1000} + 1 \right) \left(\frac{1 - \frac{25}{1000}}{1 + \frac{\delta^{13}C}{1000}} \right)^{-2} - 1 \right] * 1000$$
 (6)

2.9. Upward $CO_{2,(g)}$ flux

The flux of $CO_{2,(g)}$ from weathered bedrock to the surface is calculated following the procedure outlined in Tune et al. (2020). Briefly, Fick's law constrains CO_2 flux using the CO_2 concentration gradient and a calculated diffusion coefficient, D. The diffusion coefficient for each depth for the sampling campaigns in September and March was found using Penman's equation (Penman, 1940) using water content measurements from Well 7 in October and May via borehole neutron and nuclear magnetic resonance logging (Schmidt and Rempe, 2020). These water contents were extrapolated to the location of the VMS (Table 1), and water-inaccessible

porosity was estimated from epoxy experiments (Gu et al., 2020). Air-filled porosity was calculated from these two measurements as: $\phi_{air} = (\theta_{max} + \phi_{epoxy}) - \theta_{date}$.

2.9.1. Oxidized OC_{petro} contribution to total respired CO_2 production

As shown in Section 2.3 and Eq. (1), the binary model from Hemingway et al. (2018) was adapted to constrain the maximum percentage of total gas sample that could be attributed to respired OC_{petro} . This is accomplished by assuming F_{bio} is equivalent to the maximum $^{14}CO_{2,resp}$ we measured, such that any F values lower than this are due to some contribution of OC_{petro} oxidation. We acknowledge that this is a coarse estimate, as there are likely additional sources of OC that have a variety of ages associated with them, including aged OC from the soil. However, the simplicity of this model allows us to constrain an upper limit for the amount of OC_{petro} oxidation occurring in the upper unsaturated zone. To apply Eq. (1) to the gas phase, F_i is then set equal to the $^{14}CO_{2,(g),resp}$ constrained by our diffusion model. The rate of OC_{petro} oxidation at each depth is then the product of the total rate of respiration at each depth and X_{petro} .

3. Results

3.1. Solid phase chemistry and porosity

Organic carbon content of the weathered material ranges from 0.12 to 0.77% (Table 2). The highest value is located near the surface of the weathering profile at the soil-bedrock boundary (0.5 m). Values generally decline below this depth and vary across the

^b Values from Gu et al. (2020).

^a Depth is the average depth below the VMS well head.

b Stream bed rock concentrations from stream bed samples of unweathered rock reported in Gu et al. (2020).

Table 3 Isotopic values for solid phase samples recovered from installation of the VMS.

Depth		$\Delta^{14}C^{a}$	F_m	¹³ C
(m)		(‰)		(‰)
1.47	Above the water table year-round	-813.4 ± 0.8	0.1881 ± 0.0008	-25.1 ± 0.15
3.46	Above the water table year-round	-730.3 ± 0.8	0.2417 ± 0.0008	-24.9 ± 0.15
4.83	Above the water table year-round	-739.9 ± 0.7	0.2623 ± 0.0007	-25.1 ± 0.15
6.3	Above the water table year-round	-927.7 ± 0.6	0.0729 ± 0.0006	-25 ± 0.15
7.77	Above the water table year-round	-805.3 ± 0.7	0.1963 ± 0.0007	-25.1 ± 0.15
9.42	Within the water table fluctuation zone	-966.8 ± 0.6	0.0335 ± 0.0006	-25.5 ± 0.15
10.67	Within the water table fluctuation zone	-987.8 ± 0.5	0.0123 ± 0.0005	-25.7 ± 0.15
11.76	Within the water table fluctuation zone	-935 ± 0.6	0.0655 ± 0.0006	-25.3 ± 0.15
14.11	Within the water table fluctuation zone	-970.4 ± 0.5	0.0299 ± 0.0005	-25.8 ± 0.15
15.41	Below the water table year-round	-979.5 ± 0.5	$0.0207{\pm}0.0005$	-25.9 ± 0.15

^a ± AMS analytical uncertainty.

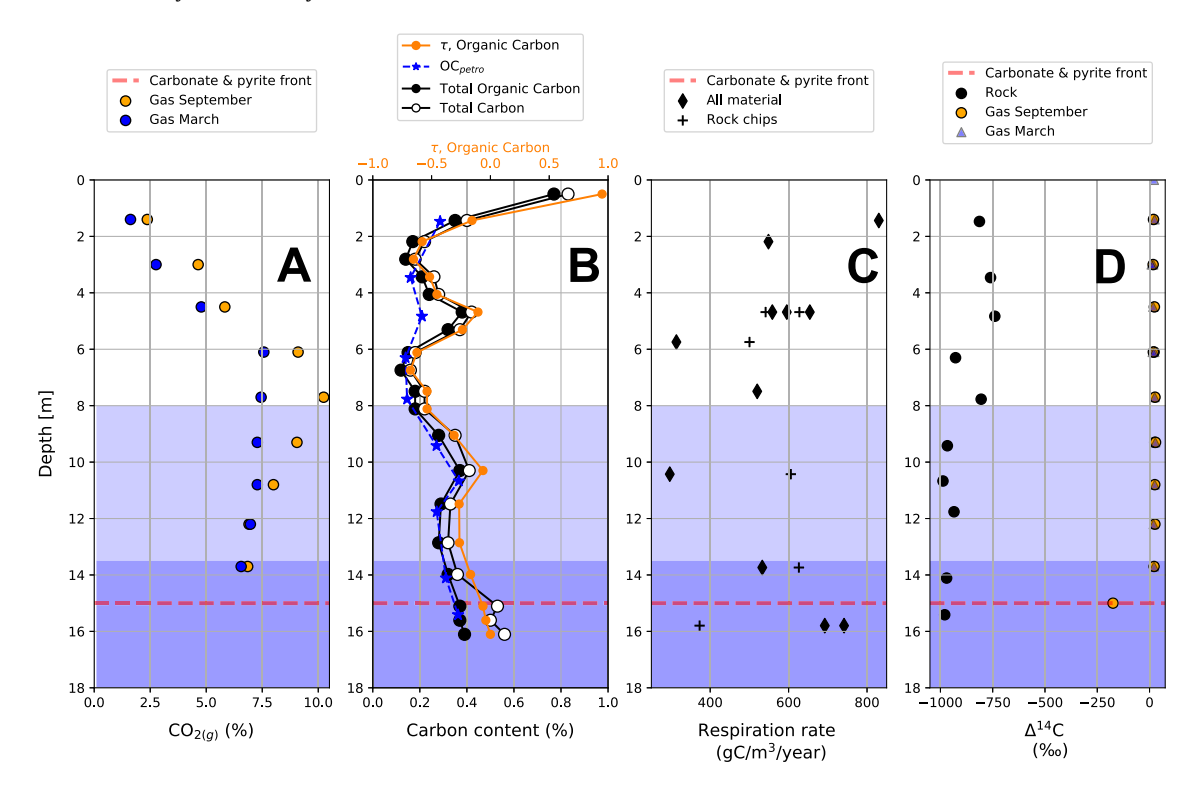


Fig. 2. Depth profiles of weathered bedrock properties at the location of the VMS. The dark shaded region in the figure denotes the depths at which the weathering profile is below the maximum depth of the water table and the lighter shaded region denotes the depths where the water table rises and lowers seasonally. A) $CO_{2,(g)}$ results from the September, 2018 and March, 2019 sampling dates. B) Total, organic and petrogenic carbon content of the solid phase recovered from VMS installation along with τ_{OC} . C) Respiration rate of incubation experiments for various depths and materials at hour 230 for each incubation (Table 4.) Note that respiration rates from incubation experiments are reported in $gC/m^3/y$ for comparison to estimates from the depth profile. D) Radiocarbon concentrations of solid and gas phase samples. $\Delta^{14}C$ values of gas samples in September and October are very similar and appear to plot on top of each other in this figure.

profile. Three minima are observed at 2.8 m (0.14%), 6.7 m (0.12%) and 12.9 m (0.28%). At the base of the weathering profile (16.1 m), the organic carbon content is 0.39%. Generally, τ_{OC} calculations show little to no depletion of OC in the permanently saturated zone, up to 68% depletion (\pm 0.18) in the interval below the root zone where the water table seasonally fluctuates, and non-monotonic depletion and accumulation within the bedrock root zone (Fig. 2). Mobile soils show depletion.

Carbon measured in the deepest VMS solids is radiocarbon dead (Table 3). This is because the age of OC_{petro} far exceeds the half life of radiocarbon. Above 9.4 m, $\Delta^{14}C$ increases, varying between -927.7 and -730.3% over the depth interval spanning 7.7 - 1.5 m (Fig. 2). Both $\Delta^{14}C$ and organic carbon concentrations increase towards the surface. Roots extend to at least 8 m at the location of the VMS (Rempe and Dietrich, 2018; Tune et al., 2020). Therefore, the solid phase samples in the upper 8 m of the weathering profile likely include more recently fixed mineral-associated OC, root matter and other younger organic sources.

We observe a depletion in OC_{petro} content of the rock from 16.1 to 12.9 m and again from 10.3 to 6.7 m. The decrease from 10.3 to 6.7 m is complicated by the addition of younger organic carbon as indicated by a change in $\Delta^{14}C$ (Fig. 2) and the departure of calculated OC_{petro} content from total OC content (Fig. 2B). From 16.1 to 12.9 m, where solid phase OC concentrations decrease from 0.39 to 0.28% C with shallowing and there is little to no modern ^{14}C , we calculate an OC_{petro} weathering rate of 0.12 gC/m³/yr (section 2.6) using a local uplift rate of 0.2 mm/yr (Fuller et al., 2009).

Across the hillslope, the depletion of OC in the near-surface begins near the weathered-unweathered rock boundary at depths where the water table rises and lowers seasonally (Fig. S1). At these depths the VMS samples indicated negligible modern OC. Several other wells were drilled across this transition zone (see Fig. 1 and Fig. S1) and OC contents are reported by Gu et al. (2020). OC $_{petro}$ weathering rates in these locations are slightly higher than in the VMS, yielding 0.21 gC/m 3 /yr at the lower mid-slope position (Well 3), 0.40 gC/m 3 /yr at the mid-slope position (Well 14),

Table 4Weathered bedrock incubation experiments. Linearly interpolated values of the raw incubation data for CO₂ flux over time are reported in Table 4. Table 4 reports the results of the incubation experiments for all depths for up to 9.5 days, after which the respiration rate exponentially declined. Fig. 2 reports these respiration rates with depth for the incubated bedrock chips at 9.5 day (230 hrs) for the chips both with and without the fines removed.

			Cumulative time incubated (hr)						
			0	24	48	72	120	168	230
Material	Depth (m)	Replicate	CO ₂ oxion (gC/m ³ /	dation rate yr)					
Rock chips and fines	1.4	No	0.0	1039.4	1264.1	1939.7	1132.3	849.6	830.0
Rock chips and fines	2.2	No	0.0	570.6	285.3	393.0	741.3	826.7	548.6
Rock chips and fines	4.7	Yes	0.0	613.6	373.9	1292.0	1060.2	681.8	595.4
Rock chips and fines	4.7	Yes	0.0	542.1	507.5	750.4	1243.4	759.3	558.5
Rock chips and fines	4.7	Yes	0.0	498.9	295.0	674.8	1238.2	1129.1	654.1
Rock chips	4.7	Yes	0.0	1467.5	729.5	605.3	684.1	722.9	627.5
Rock chips	4.7	Yes	0.0	1422.7	622.4	542.0	582.0	638.5	541.4
Rock chips and fines	5.7	No	0.0	406.4	292.7	326.0	637.6	374.4	313.8
Rock chips	5.7	No	0.0	505.8	286.7	228.3	254.2	440.3	500.3
Rock chips and fines	7.5	No	0.0	531.6	326.3	368.1	677.0	785.4	520.0
Rock chips and fines	10.4	No	0.0	380.3	295.7	561.6	602.4	355.5	296.9
Rock chips	10.4	No	0.0	1538.2	844.5	728.9	731.3	701.2	605.7
Rock chips and fines	13.7	No	0.0	824.8	604.4	830.8	994.0	665.6	532.9
Rock chips	13.7	No	0.0	1379.3	960.8	869.8	912.5	846.4	626.2
Rock chips and fines	15.8	Yes	0.0	2942.0	1521.2	1418.0	759.8	691.3	741.4
Rock chips and fines	15.8	Yes	0.0	2164.1	1715.3	1469.6	925.5	696.5	692.2
Rock chips	15.8	No	0.0	1003.0	550.1	639.9	469.7	397.5	373.0

Table 5Carbon isotopic and concentration values for the gaseous phase.

Depth (m)	Δ ¹⁴ C ^a Sept. 2018 (‰)	Δ ¹⁴ C ^a Mar. 2019 (‰)	F _m ^a Sept. 2018	F _m ^a Mar. 2019	δ ¹³ C ^a Sept. 2018 (‰)	δ ¹³ C ^a Mar. 2019 (‰)	CO _{2,(g)} Sept. 2018 (%)	CO _{2,(g)} Mar. 2019 (%)	O _{2,(g)} Sept. 2018 (%)	O _{2,(g)} Mar. 2019 (%)
1.4	19 ± 1.8	24.2 ± 1.7	1.0274 ± 0.0018	1.0327 ± 0.0017	-20.9 ± 0.15	-23.1 ± 0.15	2.37	1.62	19.1	18.6
3	17.3 ± 1.7	17.9 ± 1.7	1.0257 ± 0.0017	1.0265 ± 0.0017	-22.6 ± 0.15	-23.2 ± 0.15	4.64	2.76	16.8	16.4
3	NaN	9.8 ± 2	NaN	1.0182 ± 0.002	NaN	-23.4 ± 0.15	NaN	2.76	NaN	16.4
4.5	23.1 ± 1.7	17.6 ± 1.7	1.0316 ± 0.0017	1.0262 ± 0.0017	-23.9 ± 0.15	-23.6 ± 0.15	5.83	4.78	15.6	11
6.1	21.6 ± 1.8	14.6 ± 2	1.0301 ± 0.0018	1.0231 ± 0.002	-23.1 ± 0.15	-22.8 ± 0.15	9.1	7.57	13.3	5
6.1	18.2 ± 1.8	23 ± 1.8	1.0266 ± 0.0018	1.0315 ± 0.0018	NaN	-22.8 ± 0.15	NaN	NaN	NaN	NaN
7.7	26 ± 1.9	24.5 ± 1.7	1.0344 ± 0.0019	1.033 ± 0.0017	-23.6 ± 0.15	-22.9 ± 0.15	10.24	7.45	12.9	7.2
9.3	24.7 ± 1.7	27.8 ± 1.7	1.0332 ± 0.0017	1.0364 ± 0.0017	-23.8 ± 0.15	-23 ± 0.15	9.05	7.28	13.6	6.8
9.3	28.7 ± 1.8	NaN	1.0372 ± 0.0018	NaN	-23.8 ± 0.15	-23 ± 0.15	9.05	7.28	NaN	NaN
10.8	25 ± 1.7	24.8 ± 1.7	1.0334 ± 0.0017	1.0333 ± 0.0017	-23.7 ± 0.15	-23.2 ± 0.15	8	7.28	14.1	7.6
12.2	25.7 ± 1.8	19.5 ± 1.6	1.0342 ± 0.0018	1.028 ± 0.0016	-24.1 ± 0.15	-23.7 ± 0.15	6.91	6.97	14.5	8.9
13.7	21.7 ± 1.8	21.2 ± 1.7	1.0301 ± 0.0018	1.0297 ± 0.0017	-24.2 ± 0.15	-23.8 ± 0.15	6.85	6.56	14.4	9.2
15	-174.8 ± 1.5	Saturated	0.832 ± 0.0015	NaN	-26.1	Saturated	1.99	Saturated	3.1	NaN

 $^{^{}a}$ \pm Analytical uncertainty.

 $0.12~gC/m^3/yr$ at the upper mid-slope position (VMS), and $0.24~gC/m^3/yr$ at the top of the slope (Well 15).

3.2. Incubation of bedrock chips

OC_{petro} is respirable at all sample depths at the position in the weathering profile did not influence the respiration rate (Fig. 2). In addition, there was no appreciable difference in respiration rate between incubation experiments of shale chips alone (average 550 \pm 100 gC/m³/yr, n = 6) and bulk material that contained both shale chips and clay particles (average 570 \pm 160 gC/m³/yr, n = 11). The respiration rate varied from 296.9 to 830.0 gC/m³/yr, with a mean of 557.1 gC/m³/yr. Respiration rates were measured in units of μ gC/g-dry-soil/hr and converted to units of gC/m³/yr by assuming a density of 2.65 g/cm³. This value is consistent with the bulk density of the solid phase samples recovered from the VMS (Table S1).

These incubation experiments were designed to constrain $CO_{2,(g)}$ production through time rather than the radiocarbon content of the respired $CO_{2,(g)}$, and hence we cannot definitively rule out contributions of modern, surface-derived carbon to these rates. However, we observe no systematic trend in rate as a function of the depth from which the sample was obtained despite the fact that total solid phase OC contents increase substantially in

the upper 2 m of the weathering profile (Fig. 2). Furthermore, we observe a relatively stable rate of $CO_{2,(g)}$ production across all samples beyond the first 24 hrs of incubation, suggesting oxidation of a relatively constant organic carbon source rather than rapid consumption of a small labile pool. In total, we take these observations as evidence that the respiration rates constrained in batch incubations of shale rock chips are reflective of petrogenic carbon oxidation under optimized conditions.

3.3. Gas phase radiocarbon

Gas phase $\Delta^{14}\text{CO}_2$ from sampling campaigns in September 2018 and March 2019 capture the end-members of water content and temperature for the weathering profile (Fig. 2 and Table 5). In September, the subsurface water content in weathered rock is low and subsurface temperature is high, whereas in March, the subsurface water content is high and temperature is low (Table 1, Tune et al. 2020). Across both sampling campaigns, $\Delta^{14}\text{CO}_{2,(g)}$ fell between 9.8 and 28.7‰ in the year-round unsaturated (1.5 to 7.7 m) and seasonally saturated (7.7 to 13.7 m) zone (Fig. 2). We note that these values are slightly higher than the contemporaneous atmospheric $\Delta^{14}\text{CO}_{2,(g)}$, suggesting respiration of OC that was incorporated into the weathering profile over approximately the last decade (based on the same linear extrapolation of Graven et al.

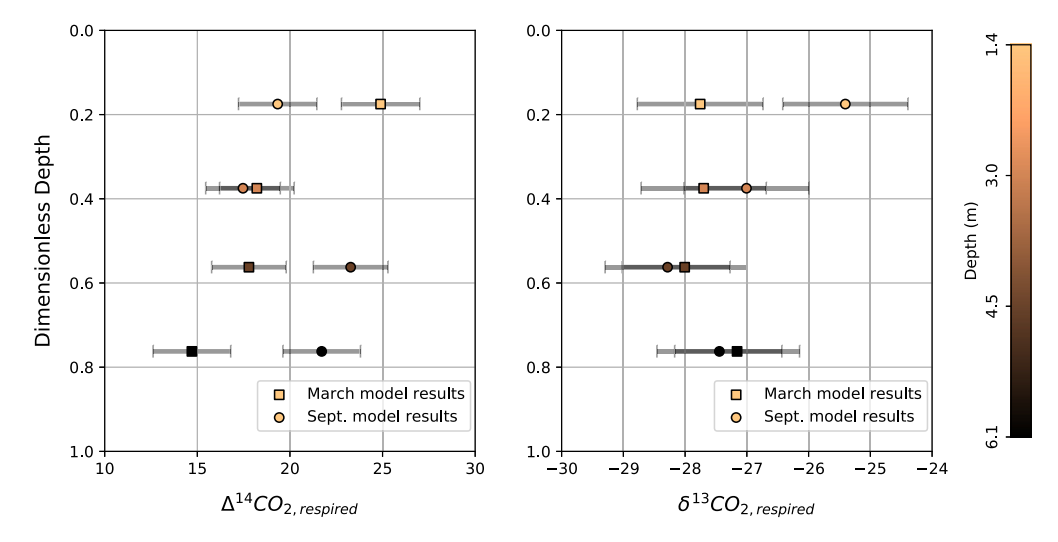


Fig. 3. Diffusion production model for radiocarbon and stable isotope value of respired $CO_{2,(g)}$, or $^{14}CO_{2,respired}$ and $^{13}CO_{2,respired}$. The $CO_{2,respired}$ values are shown as a function of dimensionless depth for each sampling date. Depths are normalized to L = 7 m (section 3.4). Error bars represent analytical uncertainty propagated through the model.

(2017) as in section 2.8.1). In the seasonally saturated zone (15 m and below), $\Delta^{14}\text{CO}_{2,(g)}$ was -174.8% at 15 m depth during the September sampling campaign. This depth (15 m) could not be sampled during the March sampling campaign due to complete water saturation of the sampling port. The sampling port at 15 m is unique not only because it is within the saturated region, but also because it samples gas and water from unweathered bedrock where there is an abrupt increase in inorganic carbon and pyrite (Fig. 2, Table 2). The porosity and geochemistry of the unweathered rock is significantly different from the weathered bedrock (Gu et al., 2020). Thus, we cannot rule out the contribution of inorganic carbon dissolution to the observed -174.8% $\Delta^{14}\text{CO}_{2,(g)}$ at 15 m depth.

3.4. Gas phase transport modeling

Eq. (5) is applied to the upper 7 m of the weathering profile to estimate the isotopic values of respired CO₂ (CO_{2,resp}, Fig. 3). The value of CO_{2,resp} differs from the pore space that is sampled in the field (CO_{2,(g)}) and measured in the laboratory (CO_{2,meas}) due to isotopic mass differences that result in unique diffusivities of $^{12}\text{CO}_{2,(g)}, \, ^{13}\text{CO}_{2,(g)}, \, \text{and} \, ^{14}\text{CO}_{2,(g)}.$ In March, $\Delta^{14}\text{CO}_{2,resp}$ is lower than $\Delta^{14}\text{CO}_{2,resp}$ in September at 4.5 and 6.1 m, indicating that older organic carbon sources may be respired when the subsurface is wet and O_{2,(g)} is lower. In September, $\Delta^{14}\text{CO}_{2,resp}$ values do not exhibit a clear trend with depth while in March, $\Delta^{14}\text{CO}_{2,resp}$ values decrease with depth indicating a greater contribution of CO_{2,(g)} produced from older OC sources.

Less than 1% of the total $CO_{2,resp}$ could derive from OC_{petro} based on the binary model used by Hemingway et al. (2018) (section 2.9.1; Fig. 4). This is true across both sampling campaigns. In March, when the subsurface is approaching maximum water contents, there is an increase in $CO_{2,resp}$ from 1.5 to 6 m for which the fraction attributed to OC_{petro} oxidation could be 0-0.99% (\pm 0.014% propagated error). In September, when the subsurface is approaching minimum water contents, the maximum contribution of OC_{petro} oxidation to $CO_{2,resp}$ has a narrower range (0.17 - 0.74%) and is greatest between 1.5 to 3 m.

This small fractional contribution of OC_{petro} oxidation in the upper weathered bedrock vadose zone could constitute as much as 0.36 gC/m³/yr at any one depth. Integrated from 1.5 to 6 m, this represents an OC_{petro} oxidation flux of 0.47 gC/m²/yr in March and 0.87 gC/m²/yr in September. Note here oxidation rates of OC_{petro}

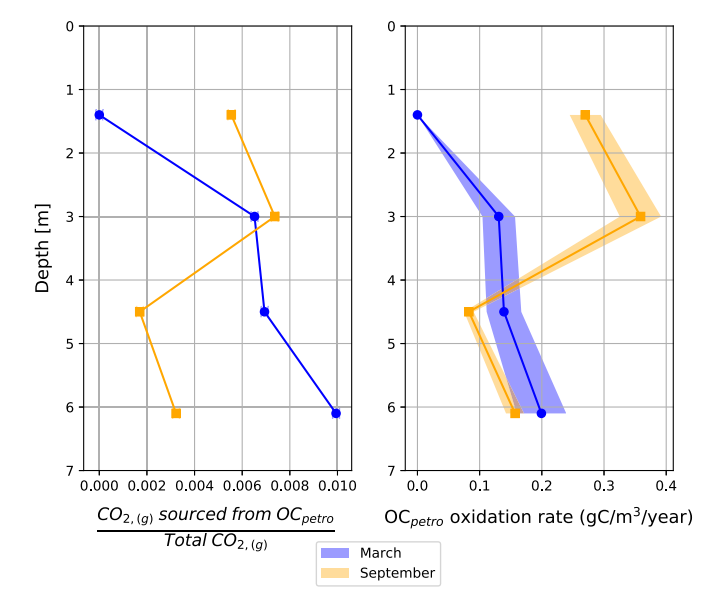


Fig. 4. Estimates of maximum possible $OC_(petro)$ oxidation in the upper 7 m of unsaturated, weathered bedrock. (left) The maximum fraction of $CO_{2(g)}$ that could originate from the oxidation of OC_{petro} based on the diffusion-corrected $^{14}CO_{2,resp}$ values. The amount of $CO_{2(g)}$ from OC_{petro} is shown as a fraction of total $CO_{2(g)}$. (right) The maximum amount of OC_{petro} that could be oxidized at each depth if total respiration is equally distributed between each depth interval ($%CO_{2,(g)}$ from OC_{petro} x CO_2 production rate). The shaded regions are the OC_{petro} oxidation rates considering an air-filled porosity between 5 and 10%, as reported in Tune et al. (2020). The lines are the OC_{petro} rate from the calculated air-filled porosity shown in Table 1.

for a volume of rock at one location are expressed as $gC/m^3/yr$ while fluxes over a depth interval are given in $gC/m^2/yr$. These estimates of OC_{petro} oxidation are roughly comparable to our estimates of OC_{petro} weathering in the lower portion of the bedrock vadose zone calculated from the solid phase analysis. Furthermore, in March, the gaseous flux of $CO_{2(g)}$ from the weathered bedrock to the atmosphere constrained by the CO_2 concentration gradient is only a portion of the total CO_2 respired in the subsurface. The remainder is solubilized and transported in the water draining through the weathering profile (Tune et al., 2020).

4. Discussion

4.1. OCpetro removal in weathered bedrock

We estimate an OC_{petro} weathering rate of 0.12 gC/m³/yr at the base of the VMS based on the change in solid phase OC content with depth (Table 2) and the average uplift rate for the site (0.2 mm/yr (Fuller et al., 2009)). This value is comparable to estimates of 0.21, 0.40 and 0.24 gC/m³/yr in Wells 3, 14, and 15, respectively. The variability across these locations may be attributed to heterogeneity in the OC content of the slightly metamorphosed turbidite sequences composing the bedrock. For example, the radiocarbon dead OC content measured at the base of the VMS (0.32-0.39 w.t.%, Table 2) is lower than the parent rock OC content of 0.59 ± 0.15 w.t.% reported by Gu et al. (2020) and falls outside of their 1σ standard deviation based on boreholes collected across the hillslope and from the Elder Creek stream bed. However, it is unlikely that this heterogeneity could create the observed significant and systematic change in OC concentration with depth across all of our drill cuttings. Systematic decreases in organic carbon are observed in shale weathering profiles despite the presence of parent rock heterogeneities (e.g. Pedrazas et al., 2021; Gu et al., 2020).

Using the documented uplift rate and the calculated OC_{petro} weathering rate of 0.12 gC/m³/yr, we estimate that 13% of OC_{petro} originally present in the bedrock is delivered to the soil surface. The incorporation of aged modern OC which originated from the surface limits our ability to confirm this estimate (Fig. 2). However, it suggests that OC_{petro} delivery to soils from the deeper weathering profile is feasible and could occur at the site. In the central range of Taiwan, Hemingway et al. (2018) found that the majority of OC_{petro} loss occurs within soils in steep, forested mountain terrain (Hovius et al., 2000). Here, our observations demonstrate that there is significant loss of OC_{petro} in the rock deeper in the weathering profile before it is converted to soils.

This rate of OC_{petro} weathering from the bedrock is calculated as a difference in OC content between two solid phase samples at depths below the influence of modern OC inputs and is therefore independent of any specific definition of unweathered bedrock composition. While solids from the base of the VMS appear to be unweathered (i.e. fresh) bedrock based on pyrite content, it is possible that some OC removal may have already occurred in these samples deeper within the saturated zone. If we were to define τ using the Gu et al. (2020) bedrock composition rather than the base of the VMS, the deepest sample from the VMS profile would be -0.31. At present we cannot differentiate between bedrock OC heterogeneity and removal in the saturated zone, or constrain the depth interval over which this removal may have occurred. However, we do note that removal of OC_{petro} in the saturated zone is consistent with evidence for silicate mineral reactivity in the saturated zone based on stable lithium isotopes and reactive transport modeling (Golla et al., 2021, 2022). Additionally, water saturated conditions promote different carbon degradation pathways (Lavy et al., 2019) that may favor OCpetro as a carbon source, and the differing mechanical strength of organic matter within unweathered shales has been shown to promote exposure of OCpetro through fracturing (Daigle et al., 2017). Therefore, we do not rule out the possibility of OC_{petro} weathering at depths greater than the pyrite oxidation front.

If we assume that the OC_{petro} removal rate calculated from the solid phase depletion of 0.12 gC/m³/yr occurs along the length of the weathering profile (14 m), this would amount to a flux of 1.68 gC/m²/yr of OC_{petro} weathered from the bedrock vadose zone, or 1.68 tonC/km²/yr. We cannot definitively attribute this OC_{petro} weathering rate to oxidation, but we can ask if this rate compares to independent estimates of oxidation based on a linear correlation between suspended sediment yield and OC_{petro} oxida-

tion rate (Hilton and West, 2020). We lack a suspended sediment load estimate specifically for Elder Creek, but this is a tributary of the South Fork of the Eel River, which has a historical suspended sediment load average of 2900 t/km²/yr (Brown and Ritter, 1971). This value, when paired with our weathering flux of 1.68 gC/m²/yr, lies outside the linear relationship between OCpetro weathering and suspended sediment yield that was generated from field observations at other locations (Hilton and West, 2020). This result should be contextualized by the fact that the Elder Creek watershed area makes up only a small percentage of the total South Fork Eel River drainage basin and therefore has a smaller suspended sediment yield. In addition, the importance of rapid mass wasting events to OCpetro liberation is not explicitly considered in the Hilton and West (2020) trend. The Franciscan Complex underlying our site is particularly prone to landslides which may be a more efficient way to remove OC_{petro} from the hillslope at this location.

Our in situ OCpetro weathering rates are orders of magnitude lower than the oxidation rates constrained by our incubation experiments (average 557.1 gC/m³/yr). At the rate of the incubation experiments, complete removal of the OCpetro content at the base of the VMS would occur in 17 yrs. Unsurprisingly, the conditions of this laboratory incubation promoted OC_{petro} oxidation rates that are enhanced relative to the field, likely due to the greater availability of oxygen in the laboratory setting and pulverization of rock chips generating greater surface area. The resulting rate of respiration derived from the incubation experiments (557.1 gC/m³/yr) should be considered a representative value for the maximum possible OC_{petro} oxidation (at 0.6 water saturation, atmospheric oxygen and high surface area). Though clearly artificially induced, this incubated respiration rate is an important result in that it shows that respiration of OCpetro is possible at water saturation states representative of the weathering profile if given sufficient oxygen and surface area. In-situ conditions that protect OCpetro from oxidation influence field oxidation rates at our site, thus providing an important constraint for future model development. Field OC_{petro} weathering rates are approximately 0.02% that of the incubationderived oxidation rates. Furthermore, the in situ OC_{petro} weathering rate in our field site is co-located with $O_{2,(g)}$ concentrations that vary between 6.8 and 14.5% (Table 5), though we note this does not preclude the possibility of micro-environments in which O_{2,(g)} is limited by diffusion. Hence, incubation experiments reveal that physical exposure of OCpetro is necessary to promote oxida-

4.2. Pathways of OC_{petro} weathering

We report weathering of OCpetro, however the fate of the mobilized OC_{petro} remains challenging to determine. It is critical to identify these removal mechanism(s), because of the implications for atmospheric CO₂ and carbonic acid mediated weathering reactions. If OC_{netro} is oxidized to CO₂ within the bedrock weathering profile, it could either diffuse upward to the soil and atmosphere or solubilize in water transiting the vadose zone. Alternatively, it is possible that OCpetro could be preferentially mobilized and even solubilized in the absence of oxidation, as evidenced by riverine particulate OC draining shale landscapes (Fox et al., 2020). Dissolved rhenium in Elder Creek suggests that at least some OC_{netro} is removed from within the hillslope (Ghazi et al., 2022). However, the presence of rhenium does not necessarily discriminate between oxidative weathering within the bedrock vadose zone or other mobilization mechanisms that ultimately remove OCpetro from bedrock. The rhenium proxy approach used to estimate OCpetro oxidation from dissolved rhenium in streams and rivers assumes that when rhenium is mobilized, OCpetro is also mobilized at the $Re:OC_{petro}$ ratio in the bedrock (Jaffe et al., 2002). Many studies rely on an additional assumption that this mobilized OC_{petro} is oxidized to CO_2 (e.g., Dalai et al., 2002). While the first assumption is strongly supported by the consistent ratio of rhenium to OC_{petro} throughout different weathering profiles (Jaffe et al., 2002; Hilton et al., 2021), it is unclear if OC_{petro} is completely oxidized upstream of the point at which rhenium measurements are collected in a watershed. This assumption leaves uncertainty as to the amount of mobilized OC_{petro} that is oxidized within the terrestrial system.

Where OC_{petro} oxidation produces a substantial fraction of gas phase CO_2 , radiocarbon analysis has been successfully used to fingerprint this signal (Keller and Bacon, 1998). However, the high production rates of CO_2 at our site (Tune et al., 2020) resulting from deep rooting lead to overwhelmingly modern gas to depths of 14 m across both wet and dry seasons (Fig. 2). This surprising result is inconsistent with observations of aged radiocarbon in the $CO_{2,(g)}$ of deep vadose zone gases (Keller and Bacon, 1998) or as efflux from outcropping OC-bearing rock (Soulet et al., 2021; Roylands et al., 2022). While a modern $CO_{2,(g)}$ profile does not exclude the possibility of OC_{petro} oxidation, discerning the signature of OC_{petro} oxidation is complicated by concurrent vigorous modern carbon cycling.

Gas phase radiocarbon measurements at our site show slight deviations with depth above measurement uncertainty (Table 5). Among the variety of reasons for this variability, it is possible that some small contributions of OCpetro oxidation are being recorded. In the upper 8 m a model inspired by soil radiocarbon studies (section 3.4) suggests an estimated maximum contribution of OCpetro to CO_{resp} of 1%, yielding a maximum OC_{petro} oxidation rate of 0.36 gC/m³/yr. Although this value is consistent with the rates estimated from the deeper solid phase VMS and well samples (section 4.1), we strongly caution that there are large errors associated with the attempt to parse oxidation of OCpetro in a bedrock vadose zone overprinted by a much larger modern OC cycle. The approach assumes two OC end members, one that is petrogenic (radiocarbon dead) and one that is both recently fixed and modern. The depth interval over which the model is applied hosts roots. It is therefore highly likely that additional ages of OC are respired within the weathering profile, and this effect would lead to smaller calculated rates of OC_{petro} oxidation. More sophisticated approaches for modeling multiple OC transport, transformation and aging pathways are capable of parsing between sources of respired OC that are aged between radiocarbon dead and recently fixed OC (Druhan and Lawrence, 2021). However, additional understanding of carbon transit times in the weathered bedrock environment would be required before applying such a model to this system.

These challenges limit our ability to draw direct comparisons between rates of OCpetro oxidation reported for exposed OCbearing rock and our soil mantled, forested weathering profile. The OCpetro removal rates we report are approximately one order of magnitude lower than radiocarbon-depleted CO_{2,(g)} fluxes measured via accumulation chambers installed on outcrops of OCbearing rock in New Zealand (Roylands et al., 2022) and France (Soulet et al., 2018, 2021). The differences in measurement techniques and their respective sampling volumes further complicate direct comparison. If indeed the rate of OCpetro oxidation in the bedrock underlying a forested hillslope is lower than exposed rock lacking vegetation or soil cover, then contemporaneous oxidation of modern organic carbon may play a role in limiting the rate of OC_{petro} oxidation. Additionally, our radiocarbon analysis suggests that a larger OCpetro oxidation rate may be supported in the dry season relative to the wet season at our site. This could potentially be driven by temperature differences as suggested by recent field evidence for temperature regulation of OCpetro oxidation rates (Roylands et al., 2022; Soulet et al., 2021). However, unlike exposed rock, the weathering profile at our site experiences large seasonal differences in water content, $O_{2,(g)}$ availability, and root activity (Tune et al., 2020). Thus, we cannot conclude that any potential seasonal differences in rates of OC_{petro} oxidation result from temperature differences alone. This motivates further laboratory based incubation experiments to determine the mechanisms that regulate OC_{petro} oxidation as well as additional field studies under variable environmental conditions. Such comparisons are important given potential shifts in land cover over large scales associated with climate and land use change.

5. Conclusions

Here, we report weathering rates of OC_{petro} within a hillslope weathering profile, oxidation rates of OC_{petro} in the laboratory, and radiocarbon analyses of $CO_{2,(g)}$ and solid phase samples. OC_{petro} in this marine sedimentary bedrock can be respired in a laboratory setting at rates orders of magnitude higher than the weathering rate observed in the field. Furthermore, $O_{2,(g)}$ remains high deep within the weathering profile, particularly during seasonally dry periods (Tune et al., 2020). Therefore, the low weathering rates we constrain in-situ are not predicated on an intrinsic inability of OC_{petro} to be respired, but rather, the mechanisms that shield OC_{petro} from removal processes.

The location and rate of CO_2 production from OC_{petro} oxidation in a hillslope may affect silicate weathering, CO_2 fluxes from the land surface, and dissolved CO_2 delivery to groundwater and streamwater. Radiocarbon measurements of $CO_{2,(g)}$ were inconclusive in determining OC_{petro} oxidized within the hillslope. Instead, radiocarbon measurements revealed significant respiration of recently photosynthesized OC. Therefore, the rate of OC_{petro} oxidation within the hillslope still requires quantification. Understanding the fate of mobilized OC_{petro} , and the partitioning between oxidation in the terrestrial environment and transport of unoxidized OC_{petro} , are important for assessing the contribution of OC_{petro} weathering to atmospheric CO_2 over time.

Notably, the modern radiocarbon signature of the $CO_{2,(g)}$ conclusively demonstrates that the substantial and dynamic CO₂ production rate reported at depths of 4-8 m in Tune et al. (2020) is the result of a modern, recently fixed carbon cycle that extends meters into the weathered bedrock below soil. We highlight that despite having access to deep vadose zone gases and water, it remained challenging to study the removal and oxidation of OC_{petro}. This is likely because oxidation of OC_{petro} occurs at slow rates, while recently photosynthesized OC oxidation occurs at rapid rates. However, the co-location of rapid oxidation of modern OC and slow removal and oxidation of OC_{netro} is likely to be common and is not isolated to this field site. Root-associated respiration in bedrock is widespread (McCormick et al., 2021) and occurs in regions where OC_{petro}-containing shale is present. While rooting in bedrock is thought to promote weathering (Hasenmueller et al., 2017; Wen et al., 2021), further research is required to examine the interactions between modern carbon cycling and OCpetro weathering in part because of the limitations of studying two different sources of organic carbon in the same profile. In order to observe and assess the controls on OCpetro oxidation in the near surface, additional tools will be required that can address the disparity in oxidation rate of differently aged carbon.

CRediT authorship contribution statement

Alison Tune: Data collection, Data analysis, Data curation, Writing – Original draft preparation. **Jennifer L. Druhan:** Conceptualization, Data collection, Data analysis, Methodology. **Corey Lawrence:** Data collection, Data interpretation, Writing – Reviewing and Editing. **Daniella Rempe:** Supervision, Writing – Reviewing and Editing.

Declaration of competing interest

The authors declare that they have no known competing financial interests or personal relationships that could have appeared to influence the work reported in this paper.

Data availability

Data and analysis from this article can be found at http://www.hydroshare.org/resource/82a50af377e14df0bdb994a982b24634 (Tune et al., 2023a) and https://doi.org/10.5281/zenodo.7619193 (Tune et al., 2023b).

Acknowledgements

This research was supported by Department of Energy, Office of Science Grant no. DE-SC0019198 and National Science Foundation Grant EAR 1331940 for the Eel River Critical Zone Observatory, National Science Foundation Grant EAR 2047318, and the University of California Natural Reserve System. A.K.T. was supported by the National Science Foundation Graduate Research Fellowship and the Geological Society of America Graduate Student Research Grant Program. The authors thank M. Wolfe and W. Speiser for help with field work and Phil Bennett and Dan Breecker for conversations that improved the manuscript. Any use of trade, firm, or product names is for descriptive purposes only and does not imply endorsement by the U.S. Government.

Appendix A. Supplementary material

Supplementary material related to this article can be found online at https://doi.org/10.1016/j.epsl.2023.118048.

References

- Bouchez, J., Beyssac, O., Gally, V., Gaillardet, J., France-Lanord, C., Maurice, L., Moreira-Turcq, P., 2010. Oxidation of petrogenic organic carbon in the Amazon floodplain as a source of atmospheric CO2. Geology 38, 255–258. https://doi.org/10.1130/g30608.1.
- Breecker, D.O., Payne, A.E., Quade, J., Banner, J.L., Ball, C.E., Meyer, K.W., Cowan, B.D., 2012. The sources and sinks of CO2 in caves under mixed woodland and grassland vegetation. Geochim. Cosmochim. Acta 96, 230–246. https://doi.org/10.1016/j.gca.2012.08.023.
- Brown, W.M., Ritter, J.R., 1971. Tech. Rep., https://doi.org/10.3133/wsp1986.
- Cerling, T.E., 1984. The stable isotopic composition of modern soil carbonate and its relationship to climate. Earth Planet. Sci. Lett. 71, 229–240. https://doi.org/10. 1016/0012-821x(84)90089-x.
- Dahan, O., Talby, R., Yechieli, Y., Adar, E., Lazarovitch, N., Enzel, Y., 2009. In situ monitoring of water percolation and solute transport using a vadose zone monitoring system. Vadose Zone J. 8, 916–925.
- Daigle, H., Hayman, N.W., Kelly, E.D., Milliken, K.L., Jiang, H., 2017. Fracture capture of organic pores in shales. Geophys. Res. Lett. 44, 2167–2176. https://doi.org/10. 1002/2016g1072165.
- Dalai, T.K., Singh, S.K., Trivedi, J., Krishnaswami, S., 2002. Dissolved rhenium in the Yamuna river system and the Ganga in the Himalaya: role of black shale weathering on the budgets of Re, Os, and U in rivers and CO 2 in the atmosphere. Geochim. Cosmochim. Acta 66, 29–43. https://doi.org/10.1016/s0016-7037(01) 00747-5.
- Davidson, E.A., Trumbore, S.E., 1995. Gas diffusivity and production of CO2 in deep soils of the eastern Amazon. Tellus, Ser. B Chem. Phys. Meteorol. 47, 550–565. https://doi.org/10.3402/tellusb.v47i5.16071.
- Davidson, G.R., 1995. The stable isotopic composition and measurement of carbon in soil CO2. Geochim. Cosmochim. Acta 59, 2485–2489. https://doi.org/10.1016/ 0016-7037(95)00143-3.
- Donahue, D.J., Linick, T.W., Jull, A.J.T., 1990. Isotope-ratio and background corrections for accelerator mass spectrometry radiocarbon measurements. Radiocarbon 32, 135–142. https://doi.org/10.1017/s0033822200040121.
- Druhan, J.L., Lawrence, C.R., 2021. Development of soil radiocarbon profiles in a reactive transport framework. Geochim. Cosmochim. Acta. https://doi.org/10.1016/i.gca.2021.05.021.

- Egan, J.E., Bowling, D.R., Risk, D.A., 2019. Technical note: isotopic corrections for the radiocarbon composition of CO2 in the soil gas environment must account for diffusion and diffusive mixing. Biogeosciences (Online) 16. https://doi.org/ 10.5194/bg-16-3197-2019.
- Ernst, W., McLaughlin, R.J., 2012. Mineral parageneses, regional architecture, and tectonic evolution of Franciscan metagraywackes, Cape Mendocino-Garberville-Covelo 30/ × 60/ quadrangles, northwest California. Tectonics 31.
- Fox, P.M., Bill, M., Heckman, K., Conrad, M., Anderson, C., Keiluweit, M., Nico, P.S., 2020. Shale as a source of organic carbon in floodplain sediments of a mountainous watershed. J. Geophys. Res., Biogeosci. 125. https://doi.org/10.1029/2019jg005419.
- Fuller, T.K., Perg, L.A., Willenbring, J.K., Lepper, K., 2009. Field evidence for climatedriven changes in sediment supply leading to strath terrace formation. Geology 37, 467–470.
- Ghazi, L., Goñi, M., Haley, B.A., Muratli, J.M., Pett-Ridge, J.C., 2022. Concentrationrunoff relationships of contrasting small mountainous rivers in the Pacific Northwest, USA: insights into the weathering of rhenium relative to other weathering products. Geochim. Cosmochim. Acta 337, 106–122. https://doi.org/10.1016/j.gca.2022.09.036. https://www.sciencedirect. com/science/article/pii/S001670372200521X.
- Golla, J.K., Kuessner, M.L., Henehan, M.J., Bouchez, J., Rempe, D.M., Druhan, J.L., 2021. The evolution of lithium isotope signatures in fluids draining actively weathering hillslopes. Earth Planet. Sci. Lett. 567, 116988. https://doi.org/10.1016/j.epsl. 2021.116988.
- Golla, J.K., Bouchez, J., Kuessner, M.L., Rempe, D.M., Druhan, J.L., 2022. Subsurface weathering signatures in stream chemistry during an intense storm. Earth Planet. Sci. Lett. 595, 117773. https://doi.org/10.1016/j.epsl.2022.117773.
- Graven, H., Allison, C.E., Etheridge, D.M., Hammer, S., Keeling, R.F., Levin, I., Meijer, H.A.J., Rubino, M., Tans, P.P., Trudinger, C.M., Vaughn, B.H., White, J.W.C., 2017. Compiled records of carbon isotopes in atmospheric CO₂ for historical simulations in CMIP6. Geosci. Model Dev. 10, 4405–4417. https://doi.org/10.5194/gmd-10-4405-2017.
- Gu, X., Rempe, D.M., Dietrich, W.E., West, A.J., Lin, T.-C., Jin, L., Brantley, S.L., 2020. Chemical reactions, porosity, and microfracturing in shale during weathering: the effect of erosion rate. Geochim. Cosmochim. Acta 269, 63–100. https://doi. org/10.1016/j.gca.2019.09.044.
- Hahm, W.J., Rempe, D.M., Dralle, D.N., Dawson, T.E., Lovill, S.M., Bryk, A.B., Bish, D.L., Schieber, J., Dietrich, W.E., 2019. Lithologically controlled subsurface critical zone thickness and water storage capacity determine regional plant community composition. Water Resour. Res. 55, 3028–3055. https://doi.org/10.1029/2018WR023760.
- Hansson, A., Dargusch, P., Shulmeister, J., 2021. A review of modern treeline migration, the factors controlling it and the implications for carbon storage. J. Mt. Sci. 18, 291–306. https://doi.org/10.1007/s11629-020-6221-1.
- Hasenmueller, E.A., Gu, X., Weitzman, J.N., Adams, T.S., Stinchcomb, G.E., Eissenstat, D.M., Drohan, P.J., Brantley, S.L., Kaye, J.P., 2017. Weathering of rock to regolith: the activity of deep roots in bedrock fractures. Geoderma 300, 11–31. https://doi.org/10.1016/j.geoderma.2017.03.020.
- Hemingway, J.D., Hilton, R.G., Hovius, N., Eglinton, T.I., Haghipour, N., Wacker, L., Chen, M.-C., Galy, V.V., 2018. Microbial oxidation of lithospheric organic carbon in rapidly eroding tropical mountain soils. Science 360, 209–212. https://doi.org/ 10.1126/science.aao6463.
- Hilton, R.G., West, A.J., 2020. Mountains, erosion and the carbon cycle. Nat. Rev. Earth Environ. 1, 284–299. https://doi.org/10.1038/s43017-020-0058-6.
- Hilton, R.G., Turowski, J.M., Winnick, M., Dellinger, M., Schleppi, P., Williams, K.H., Lawrence, C.R., Maher, K., West, M., Hayton, A., 2021. Concentration-discharge relationships of dissolved rhenium in Alpine catchments reveal its use as a tracer of oxidative weathering. Water Resour. Res. 57. https://doi.org/10.1029/ 2021wr029844.
- Horan, K., Hilton, R.G., Selby, D., Ottley, C.J., Gröcke, D.R., Hicks, M., Burton, K.W., 2017. Mountain glaciation drives rapid oxidation of rock-bound organic carbon. Sci. Adv. 3, e1701107. https://doi.org/10.1126/sciadv.1701107.
- Horan, K., Hilton, R.G., Dellinger, M., Tipper, E., Galy, V., Calmels, D., Selby, D., Gaillardet, J., Ottley, C.J., Parsons, D.R., Burton, K.W., 2019. Carbon dioxide emissions by rock organic carbon oxidation and the net geochemical carbon budget of the Mackenzie River Basin. Am. J. Sci. 319, 473–499. https://doi.org/10.2475/06. 2019.02.
- Hovius, N., Stark, C.P., Hao-Tsu, C., Jiun-Chuan, L., 2000. Supply and removal of sediment in a landslide-dominated mountain belt: Central Range, Taiwan. J. Geol. 108, 73–89.
- Jaffe, L.A., Peucker-Ehrenbrink, B., Petsch, S.T., 2002. Mobility of rhenium, platinum group elements and organic carbon during black shale weathering. Earth Planet. Sci. Lett. 198, 339–353. https://doi.org/10.1016/s0012-821x(02)00526-5.
- Keller, C.K., Bacon, D.H., 1998. Soil respiration and georespiration distinguished by transport analyses of vadose CO2, 13CO2, and 14CO2. Glob. Biogeochem. Cycles 12, 361–372. https://doi.org/10.1029/98gb00742.
- LaRowe, D.E., Van Cappellen, P., 2011. Degradation of natural organic matter: a thermodynamic analysis. Geochim. Cosmochim. Acta 75, 2030–2042.
- Lavy, A., McGrath, D.G., Carnevali, P.B.M., Wan, J., Dong, W., Tokunaga, T.K., Thomas, B.C., Williams, K.H., Hubbard, S.S., Banfield, J.F., 2019. Microbial communities across a hillslope-riparian transect shaped by proximity to the stream,

- groundwater table, and weathered bedrock. Ecol. Evol. 9, 6869–6900. https://doi.org/10.1002/ece3.5254.
- Liu, Y., Lawrence, C.R., Winnick, M.J., Hsu, H.-T., Maher, K., Druhan, J.L., 2019. Modeling transient soil moisture limitations on microbial carbon respiration. J. Geophys. Res., Biogeosci. 124, 2222–2247. https://doi.org/10.1029/2018ig004628.
- McCormick, E.L., Dralle, D.N., Hahm, W.J., Tune, A.K., Schmidt, L.M., Chadwick, K.D., Rempe, D.M., 2021. Widespread woody plant use of water stored in bedrock. Nature 597, 225–229. https://doi.org/10.1038/s41586-021-03761-3.
- Murphy, C.J., Baggs, E.M., Morley, N., Wall, D.P., Paterson, E., 2015. Rhizosphere priming can promote mobilisation of N-rich compounds from soil organic matter. Soil Biol. Biochem. 81, 236–243. https://doi.org/10.1016/j.soilbio.2014.11.027.
- Pedrazas, M.A., Hahm, W.J., Huang, M.-H., Dralle, D., Nelson, M.D., Breunig, R.E., Fauria, K.E., Bryk, A.B., Dietrich, W.E., Rempe, D.M., 2021. The relationship between topography, bedrock weathering, and water storage across a sequence of ridges and valleys. J. Geophys. Res., Earth Surf. 126. https://doi.org/10.1029/2020iff065848
- Penman, H.L., 1940. Gas and vapour movements in the soil: I. The diffusion of vapours through porous solids. J. Agric. Sci. 30, 437–462. https://doi.org/10. 1017/s0021859600048164.
- Petsch, S., Berner, R., Eglinton, T., 2000. A field study of the chemical weathering of ancient sedimentary organic matter. Org. Geochem. 31, 475–487.
- Petsch, S., Eglinton, T., Edwards, K., 2001. 14C-dead living biomass: evidence for microbial assimilation of ancient organic carbon during shale weathering. Science 292, 1127–1131.
- Rasmussen, C., Heckman, K., Wieder, W.R., Keiluweit, M., Lawrence, C.R., Berhe, A.A., Blankinship, J.C., Crow, S.E., Druhan, J.L., Pries, C.E.H., Marin-Spiotta, E., Plante, A.F., Schädel, C., Schimel, J.P., Sierra, C.A., Thompson, A., Wagai, R., 2018. Beyond clay: towards an improved set of variables for predicting soil organic matter content. Biogeochemistry 137, 297–306. https://doi.org/10.1007/s10533-018-0424-3
- Rempe, D.M., Dietrich, W.E., 2014. A bottom-up control on fresh-bedrock topography under landscapes. Proc. Natl. Acad. Sci. 111, 6576–6581. https://doi.org/10.1073/pnas.1404763111.
- Rempe, D.M., Dietrich, W.E., 2018. Direct observations of rock moisture, a hidden component of the hydrologic cycle. Proc. Natl. Acad. Sci. 115, 2664–2669. https://doi.org/10.1073/pnas.1800141115.
- Roylands, T., Hilton, R.G., Garnett, M.H., Soulet, G., Newton, J.-A., Peterkin, J.L., Hancock, P., 2022. Capturing the short-term variability of carbon dioxide emissions from sedimentary rock weathering in a remote mountainous catchment, New Zealand. Chem. Geol. 608, 121024.
- Salve, R., Rempe, D.M., Dietrich, W.E., 2012. Rain, rock moisture dynamics, and the rapid response of perched groundwater in weathered, fractured argillite underlying a steep hillslope. Water Resour. Res. 48, W11528. https://doi.org/10.1029/ 2012WR012583.
- Schillawski, S., Petsch, S., 2008. Release of biodegradable dissolved organic matter from ancient sedimentary rocks. Glob. Biogeochem. Cycles 22.

- Schmidt, L., Rempe, D., 2020. Quantifying dynamic water storage in unsaturated bedrock with borehole nuclear magnetic resonance. Geophys. Res. Lett. 47. https://doi.org/10.1029/2020gl089600.
- Sharma, S., Andrus, R., Bergeron, Y., Bogdziewicz, M., Bragg, D.C., Brockway, D., Cleavitt, N.L., Courbaud, B., Das, A.J., Dietze, M., Fahey, T.J., Franklin, J.F., Gilbert, G.S., Greenberg, C.H., Guo, Q., Lambers, J.H.R., Ibanez, I., Johnstone, J.F., Kilner, C.L., Knops, J.M.H., Koenig, W.D., Kunstler, G., LaMontagne, J.M., Macias, D., Moran, E., Myers, J.A., Parmenter, R., Pearse, I.S., Poulton-Kamakura, R., Redmond, M.D., Reid, C.D., Rodman, K.C., Scher, C.L., Schlesinger, W.H., Steele, M.A., Stephenson, N.L., Swenson, J.J., Swift, M., Veblen, T.T., Whipple, A.V., Whitham, T.G., Wion, A.P., Woodall, C.W., Zlotin, R., Clark, J.S., 2022. North American tree migration paced by climate in the West, lagging in the East. Proc. Natl. Acad. Sci. 119, e2116691118. https://doi.org/10.1073/pnas.2116691118.
- Soulet, G., Hilton, R.G., Garnett, M.H., Dellinger, M., Croissant, T., Ogrič, M., Klotz, S., 2018. Technical note: in situ measurement of flux and isotopic composition of CO₂ released during oxidative weathering of sedimentary rocks. Biogeosciences 15, 4087–4102. https://doi.org/10.5194/bg-15-4087-2018.
- Soulet, G., Hilton, R.G., Garnett, M.H., Roylands, T., Klotz, S., Croissant, T., Dellinger, M., Bouteiller, C.L., 2021. Temperature control on CO2 emissions from the weathering of sedimentary rocks. Nat. Geosci. 14, 665–671. https://doi.org/10.1038/s41561-021-00805-1.
- Stuiver, M., Polach, H.A., 1977. Discussion reporting of 14C data. Radiocarbon 19, 355–363. https://doi.org/10.1017/s0033822200003672.
- Tecon, R., Or, D., 2017. Biophysical processes supporting the diversity of microbial life in soil. FEMS Microbiol. Rev. 41, 599–623. https://doi.org/10.1093/femsre/ fux039.
- Tune, A.K., Druhan, J.L., Wang, J., Bennett, P.C., Rempe, D.M., 2020. Carbon dioxide production in bedrock beneath soils substantially contributes to forest carbon cycling. J. Geophys. Res., Biogeosci. 125. https://doi.org/10.1029/2020jg005795.
- Tune, A., Druhan, J.L., Lawrence, C.R., Rempe, D.M., 2023a. Dataset for "Deep root activity overprints weathering of petrogenic organic carbon in shale". HydroShare. http://www.hydroshare.org/resource/82a50af377e14df0bdb994a982b24634.
- Tune, A.K., Druhan, J.L., Lawrence, C.R., Rempe, D.M., 2023b. Code for manuscript: Deep root activity overprints weathering of petrogenic organic carbon in shale (Version v1.0.0) [Computer software]. https://doi.org/10.5281/zenodo.7619193.
- Turkeltaub, T., Kurtzman, D., Bel, G., Dahan, O., 2015. Examination of groundwater recharge with a calibrated/validated flow model of the deep vadose zone. J. Hydrol. 522, 618–627.
- Wen, H., Sullivan, P.L., Macpherson, G.L., Billings, S.A., Li, L., 2021. Deepening roots can enhance carbonate weathering by amplifying CO₂-rich recharge. Biogeosciences 18, 55–75. https://doi.org/10.5194/bg-18-55-2021.
- West, A.J., Galy, V., Torres, M., Ponton, C., Feakins, S.J., 2019. Field constraints from the Amazon basin reveal a rapid rate constant for oxidation of rock-derived organic carbon. In: American Geophysical Union, Fall Meeting 2019, Abstract #B41H-2481. 2019AGUFM.B41H2481W.